



Research Article

Analytic and numerical results of a disc cam bending with a roller follower

Louay S. Yousuf¹ · Dan B. Marghitu¹

Received: 26 January 2020 / Accepted: 20 August 2020 / Published online: 7 September 2020
 © Springer Nature Switzerland AG 2020

Abstract

The bending deflection of a disc cam with a roller follower was analyzed by using constant angular velocity of the cam. The objective of this paper was to study the effect of the contact load on the bending deflection of the cam profile. Numerical simulations were carried out using SolidWorks and ANSYS Ver. 19.2 package based on finite element analysis. SolidWorks was used to determine the dynamic response of the follower, while the bending deflection of the cam profile has been investigated using ANSYS package. The modal and harmonic analyses were used to find the natural frequency and the dynamic response of the bending deflection. The theory of circular plate was applied to derive the analytic solution for the bending deflection. The experiment data has been collected with an infrared camera system. The dynamic response of the follower, at the point of contact, was verified analytically and experimentally. The reduction rate for bending deflection is (73.425%) for path no. (1), (85.925%) for path no. (2), and (61.467%) for path no. (3). The harmonic amplitude peak of the point (18) on the nose (2) is bigger than the peak of the point (4) on the nose (1) because of large values for the radius of curvature of the nose (2).

Keywords Circular plate theory · Bending deflection · Contact load · ANSYS package

Nomenclature

P	Contact force between cam and follower, N	x_c	Analytic dynamic response for the follower, mm
k_1	Stiffness of the preload spring, N/mm	L	Length of the cam and follower along z-axis, mm
Δ	Spring extension due to the preload external force, mm	P_o	Maximum contact load per unit length, N/mm
k, c	Spring stiffness and viscous damping coefficient, N/mm, N s/mm	a_1, b_1	Major and minor axis of the Hertzian contact ellipse, mm
x, \dot{x}, \ddot{x}	Linear displacement, velocity, and acceleration of the roller follower, mm, mm/s, mm/s ²	m_1, n_1	Functions of the geometry of the contact surfaces
w	Weight of roller follower, N	R_1, R_2	Radii of curvatures of contacting cam and follower, mm
m	Mass of roller follower, kg	R'_1, R'_2	Principal radii of relative curvature, mm
g	Gravitational acceleration, mm/s ²	ν_1, ν_2	Poisson's ratio for cam and follower respectively
Ω	Cam angular velocity, rad/s	E_1, E_2	Modulus of elasticity for both cam and follower respectively, N/mm ²
t	Time of contact including the time of the dwell stroke, s		
X_{st}	Static deflection, mm		

✉ Louay S. Yousuf, louaysabah79@yahoo.com | ¹Department of Mechanical Engineering-Wiggins Hall, Auburn University, 354 War Eagle Way, Auburn, AL 36849, USA.



SN Applied Sciences (2020) 2:1639 | <https://doi.org/10.1007/s42452-020-03383-w>

v_{x_o}, v_{x_f}	Initial and final tangential velocities before and after the contact respectively, mm/s
v_{y_o}, v_{y_f}	Initial and final normal velocities before and after the contact respectively, mm/s
ψ	Pressure angle between cam and follower, degree
α	Angle between the planes containing curvatures $\frac{1}{R_1}$ and $\frac{1}{R_2}$, degree
R_b	Radius of the base circle, mm
$M_r, M_\theta, M_{r\theta}$	Circular bending and twist moments, N mm
ρ	Disc cam density, kg/mm ³
D	Bending rigidity, N mm
r	Radius of curvature at any point of the cam profile, mm
w	Bending deflection at the point of contact and it is varied with respect to (r, θ, t) , mm
ω_n	Natural frequency of the cam, rad/s
R_p, θ_p	Radius of curvature and angle of contact at the point of contact, mm and degree respectively
r_1	Hub radius, mm
t_1	Time at any angle of contact θ_p excluding the time of the dwell stroke, s
N	Cam angular speed, rpm

1 Introduction

The disc cam with the roller follower mechanism is extensively used in machine tools, paper processing machines, automatic assembly lines, packing machine, and many automated manufacturing devices. This paper studies the problem how to calculate the bending deflection of a cam profile at the contact point. The contact between the cam and the follower is a small elliptical or semi-ellipsoid region which exhibits a very high contact stress. The study of the contact is important for keeping the noise and the vibrations as low as possible at high speed. Sundar et al. [1] used Hertzian contact theory to calculate the contact stiffness at the point of contacts. They analyzed numerically the coefficient of restitution. The Hertzian laws were used with a damping term to accommodate the energy loss during the impact [2]. The stiffness model for the active and dwell periods of the globoidal cam was used by Kuang et al., to characterize the mesh stiffness fluctuation due to the contact [3]. They investigated the correlation between the dynamic response of the globoidal cam system and the motor driving speed numerically and experimentally. A concave-convex surface of contact had been selected between the cam and follower to suppress the high contact forces at high speeds. Hsieh employed

a conjugate surface theory to derive a kinematic model of the cam mechanism taking into consideration a negative radius of the roller follower [4]. The Hertz contact theory of stress analysis is crucial for improving the contact fatigue life cycles of the cam-follower system. Hua et al., found that the smooth surface of cam profile provides a 53% reduction in maximum subsurface Von Mises stress [5]. Contact stress can be reduced to 41% experimentally taking into consideration the dwell stroke for a constant velocity of the cam [6]. SolidWorks, Cosmosmotion and Algor softwares were used by Ghazalli to determine the stress concentration at the point of contact using the finite element analysis [7]. Fabien et al., selected a dwell-rise-dwell cam profile to reduce the peak of the contact stress over a range of speeds [8]. They derived the displacement of a translating flat-face follower with free of cusp and presented the design of a cam profile using higher order of B-spline functions [9]. Angeles et al., calculated the contact pressure with a series of harmonic waves of local deformation and sub-surface stress fields [10]. Optimal-control-theory was used by Chew et al., to optimize the contact stress and the pressure angle for D–R–D and D–R–R–D cam profiles [11]. Pandey et al., used the finite element method (ANSYS Ver. 14) to calculate the deflection and the stress distribution of a disc cam and knife edge follower [12, 13]. Tsiafis et al., studied the effect of eccentricity on the pressure angle and contact stress of a cam with a flat-faced follower mechanism by using a genetic algorithm [14]. Patel changed the flat-face of the follower to a curved face to obtain the required contact stress experimentally and analytically [15]. He observed that the contact stress value of both modified and existing roller follower remains almost the same. This study had been organized in the following steps: (i) in Sects. 2 and 3, the experiment setup was done to investigate the nonlinear dynamic response of the follower at the point of contact through an OPTOTRAK/3020 device. (ii) In Sect. 4, the analytic solution of the follower response was presented by using single-degree-of-freedom system. (iii) In Sect. 5, the contact parameters had been entered to SolidWorks software in order to calculate follower displacement, velocity, and acceleration of the impact phenomenon. (iv) In Sects. 6 and 7, both elements (PLANE42) and (SHELL99) were used in ANSYS package to determine the bending deflection numerically, while elements (TARGE170) and (CONTA174) were presented to describe the contact analysis. (v) The formulation of the contact load had been discussed as depicted in Sect. 8. (vi) In Sect. 9, the mesh convergence was carried out to find the exact value of bending deflection. (vii) The analytic solution of the bending deflection had been shown in Sect. 10 by using the theory of circular plate.

2 Experiment setup

An elastic spring was used to retain the two mechanical parts in permanent contact. The experiment setup was employed for the data acquisition with a signal processing approach. The follower motion requires a marker in a return loop to assure that the object reaches its position [16]. The motion of the follower was processed experimentally with the infrared 3-D camera device. The camera device has a control unit to track the follower movement. Figure 1 shows the experiment setup of the cam-follower test rig.

3 Experiment measurements

Data acquisition technique through signal processing approach was used to measure the contact load [17, 18]. Macro sensors were attached to the cam and the follower. The macro sensors are linear variable differential transformer (LVDT), model number (DC750-5001), and Trans-Tek linear velocity transformer (LVT), model number (0112-00002) [19]. The optical marker (macro sensor) adjusts either the absolute or the incremental movement of the follower at the contact point. The LVDT sensor transforms the analog signal (voltage pulse) into a digital signal [20].

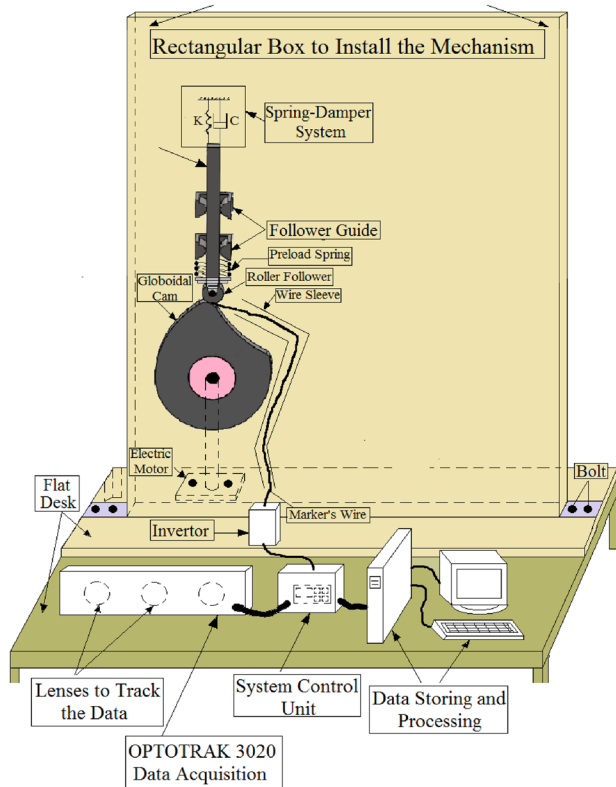


Fig. 1 Experiment rig test

The infrared markers, used with OPTOTRAK/3020, track the follower movement by taking into account the spring-damper system at the end of follower stem. The follower movement was processed with three infrared cameras. From the follower experimental displacement we can calculate the velocity $\dot{x}(t)$ and acceleration $\ddot{x}(t)$. The contact load has the expression:

$$P = k_1(\Delta + x(t)_{\text{experiment}}) - kx(t)_{\text{experiment}} - c\dot{x}(t)_{\text{experiment}} - \frac{W}{g}\ddot{x}(t)_{\text{experiment}}$$

4 Analytic solution of the dynamic response

The spring-damper system decreases the bending deflection of the cam at the point of contact since it absorbs the vibrations of cam-follower mechanism [21]. The follower has a simple harmonic motion. The cam-follower mechanism had one degree of freedom system [22]. The mechanism, shown in Fig. 2, has the mass $m = 0.2759$ kg, the spring stiffness $k = 7$ N/mm, and the viscous damper coefficient $c = 0.875$ N s/mm [23]. The equation of motion of the cam-follower mechanism is:

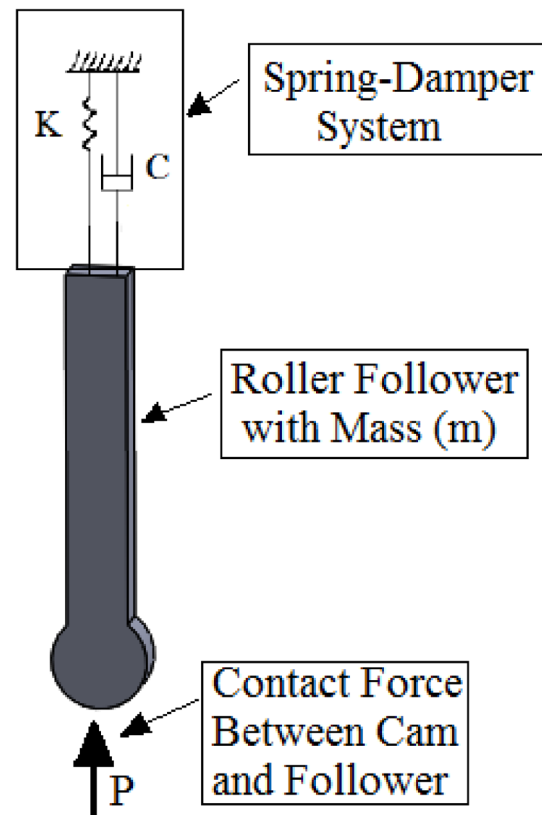


Fig. 2 One-degree-of-freedom system [22]

$$\ddot{x} + \frac{cg}{w}\dot{x} + \frac{kg}{w}x = F \sin(\Omega t), \tag{1}$$

where:

$$\frac{cg}{w} = 2\beta, \frac{kg}{w} = \omega^2, F = p \frac{g}{w}.$$

After simplification the equation of motion will be:

$$\ddot{x} + 2\beta\dot{x} + \omega^2x = F \sin(\Omega t). \tag{2}$$

The homogeneous solution of Eq. (2) is:

$$x_H = e^{-\beta t} [C_1 \sin(\sqrt{\omega^2 - \beta^2}t) + C_2 \cos(\sqrt{\omega^2 - \beta^2}t)]. \tag{3}$$

The particular solution of Eq. (2) is:

$$x_p = C_3 \sin(\Omega t) + C_4 \cos(\Omega t), \tag{4}$$

where: $C_1, C_2, C_3,$ and C_4 are constants. The first and second derivatives of Eq. (4) are:

$$\dot{x}_p = \Omega C_3 \cos(\Omega t) - \Omega C_4 \sin(\Omega t)$$

and,

$$\ddot{x}_p = -\Omega^2 C_3 \sin(\Omega t) - \Omega^2 C_4 \cos(\Omega t)$$

Substitute x_p, \dot{x}_p and \ddot{x}_p into Eq. (2) we obtain:

$$C_3 = \frac{X_{st}}{H} \left[1 - \left(\frac{\Omega^2}{\omega^2} \right) \right]$$

and

$$C_4 = -\frac{X_{st}}{H} \frac{2\beta\Omega}{\omega^2},$$

where

$$X_{st} = \frac{F}{\omega^2},$$

$$H = \left[1 - \left(\frac{\Omega^2}{\omega^2} \right) \right]^2 + \frac{4\beta^2\Omega^2}{\omega^4}.$$

The complimentary solution is:

$$x_C = x_H + x_p. \tag{5}$$

Substituting Eqs. (3) and (4) into Eq. (5) we obtain:

$$x_C = e^{-\beta t} (C_1 \sin(\sqrt{\omega^2 - \beta^2}t) + (C_2 \cos(\sqrt{\omega^2 - \beta^2}t) + \frac{X_{st}}{H} [1 - (\frac{\Omega^2}{\omega^2})] \sin(\Omega t) - \frac{X_{st}}{H} \frac{2\beta\Omega}{\omega^2} \cos(\Omega t)). \tag{6}$$

The constants C_1 and C_2 are calculated from the initial boundary conditions as illustrated below:

B.C.(1) at $t = 0, x_C = 0$, B.C.(2) at $t = 0, \dot{x}_C = 0$.

After applying the boundary conditions on Eq. (6) the constants C_1 and C_2 are:

$$C_1 = \frac{\Omega X_{st} \left[\frac{\Omega^2}{\omega^2} + \frac{2\beta^2}{\omega^2} - 1 \right]}{H \sqrt{\omega^2 - \beta^2}},$$

$$C_2 = \frac{2X_{st}\beta\Omega}{H\omega^2}.$$

The general solution of follower response is:

$$x_C(t) = e^{-\beta t} \left[\frac{\Omega X_{st} \left[\frac{\Omega^2}{\omega^2} + \frac{2\beta^2}{\omega^2} - 1 \right]}{H \sqrt{\omega^2 - \beta^2}} \sin(\sqrt{\omega^2 - \beta^2}t) + \frac{2X_{st}\beta\Omega}{H\omega^2} \cos(\sqrt{\omega^2 - \beta^2}t) \right] + \frac{X_{st}}{H} \left[1 - \left(\frac{\Omega^2}{\omega^2} \right) \right] \sin(\Omega t) - \frac{X_{st}}{H} \frac{2\beta\Omega}{\omega^2} \cos(\Omega t). \tag{7}$$

5 Numerical simulation for the contact model

SolidWorks was used to build and analyze the disc cam, the roller follower, and the two guides [24]. The spring has the elastic constant ($k_1 = 38.0611$ N/mm), the length ($l = 28$ mm), the spring index ($C_{index} = 7$), the preload extension ($\Delta = 37$ mm), the coil diameter ($d = 0.8$ mm) and the outside diameter ($OD = 6.4$ mm). The spring force is an external force in SolidWorks to keep the cam and follower in permanent contact. The spring force was applied at the point of coordinates $x = 0, y = 161.76$ mm, $z = 0$. The expression of the contact force at is [25]:

$$P = k_1(\Delta + x(t)) - kx(t) - c\dot{x}(t) - \frac{W}{g}\ddot{x}(t). \tag{8}$$

The spring and the damper were located at the end of the follower stem of coordinates $x = 0, y = 227.79$ mm, $z = 0$. The contact between a disc cam and roller follower with the dimensions is illustrated in Fig. 3.

The area of contact can be assumed to be semi-ellipsoid with a rectangular contact zone of half-width b and length L (contact between two parallel cylinders) [26]:

$$b = K_b \sqrt{P}, \tag{9}$$

where:

$$K_b = \sqrt{\left(\frac{2}{\pi L} \right) \frac{(1 - \nu_1^2)/E_1 + (1 - \nu_2^2)/E_2}{(1/d_1 + 1/d_2)}}.$$

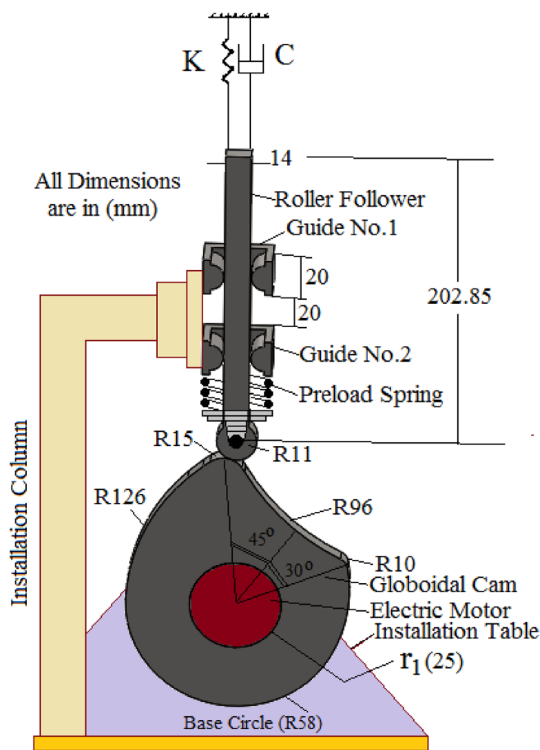


Fig. 3 Contact between a disc cam and a roller follower [3]

The maximum depth z underneath the surface of contact is calculated with $\frac{z}{b} = 0.786$, and [26, 27]

$$\zeta = \frac{z}{b} \tag{10}$$

Both the cam and the follower made from medium carbon steel with ($E_1 = E_2 = 206$ GPa) and ($\nu_1 = \nu_2 = 0.29$). The hardness is defined as the resistance of a material to permanent deformation during application of load. The bending deflection and the contact load are both significantly small because of high values of the hardness.

The penetration distance δ is [28]:

$$\delta = \frac{2P(1 - \nu^2)}{\pi LE} \left[\frac{2}{3} + \ln \frac{4R_1}{b} + \ln \frac{4R_2}{b} \right], \tag{11}$$

where: $\frac{1}{E} = \frac{1 - \nu_1^2}{E_1} + \frac{1 - \nu_2^2}{E_2}$

($\nu_1 = \nu_2 = \nu$), and, ($E_1 = E_2$)

The impact follower velocity is

$$V_C = \sqrt{2g\Delta h}. \tag{12}$$

The Hertzian contact theory predicts the value of the exponent n based on the flattening. The exponent value

n is ranging from 1.5 for (spherical punch) to 2 for (wedge shaped punch) [26, 29].

The effective kinetic coefficient of friction was calculated from the tangential (velocity in the x -direction) and the normal velocity (velocity in the y -direction) before and after the contact. The kinetic coefficient of friction is as below [29].

$$\mu_k = \frac{m[v_{x_f} - v_{x_o}]}{m[v_{y_f} - v_{y_o}]}$$

The contact parameters such as the contact force (p), contact bodies stiffness (K_b), damping ratio (ζ), penetration (δ), sliding contact velocity (V_C), exponent (n), and the kinetic coefficient of friction (μ_k) are input data for Solid-Works simulations.

6 Numerical simulation for the bending deflection of the cam

The numerical simulation of bending deflection has been done by using ANSYS Ver. 19.2 package [30]. The linear elastic isotropic model was used to calculate the bending deflection of cam profile. The element (PLANE 42) was assigned to create the mesh generation of finite element analysis. This element was defined by four nodes with two degrees of freedom at each node: (translations in the nodal x, y directions). The translation degrees of freedom were assumed to be zero (clamped boundary conditions) at the hub radius when ($r = r_1$). For the contact analysis, the element (TARGE 170) and the element (CONTA 174) have been used to create the mesh between the target and the contact surfaces. The disc cam represents the source, while the roller follower is the target. The simulation was done in two steps. For the first step, a small displacement was imposed on the target surface because of the small value of the radius of curvature. For the second step, the small imposed displacement was deleted and the force was applied at the point of contact. The modal and harmonic analyses were performed to find the natural frequency and the dynamic response of bending deflection respectively. The element (PLANE 42) can be used in modal analysis to extract the value of the natural frequency. The value of the natural frequency has been entered to the harmonic analysis by taking into consideration the use of element (SHELL99) instead of element (PLANE42) since (SHELL99) has eight nodes. The harmonic analysis tied with the modal analysis based on the natural frequency. Both the element (PLANE42) and the element (SHELL99)

are appropriate to calculate cam bending deflection. The impact of the follower has been done using SolidWorks. The displacement and the velocity of the follower were used to calculate the value of pressure angle. The pressure angle was used to find the maximum contact load (P_o). The maximum contact load was used in ANSYS package (FE model) to calculate the bending deflection. Figure 4a show the mesh generation of the finite element analysis for the disc cam and roller follower. Figure 4b show the refined and optimized mesh density.

The profile of the disc cam was divided into three paths at the point of contact:

- Path no. (1): [nose(1), flank(1), and nose(2)].
- Path no. (2): [flank(2), and nose(1)].
- Path no. (3): [nose(2), and flank(3)].

The path no. (1) was formed by the points (4, 7, 10, 12, 15, 18), while the path no. (2) was formed by the points (4, 72, 70, 68, 66, 64), as shown in Fig. 5. The path no. (3) was defined by the points (18,24,26,28,30,32).

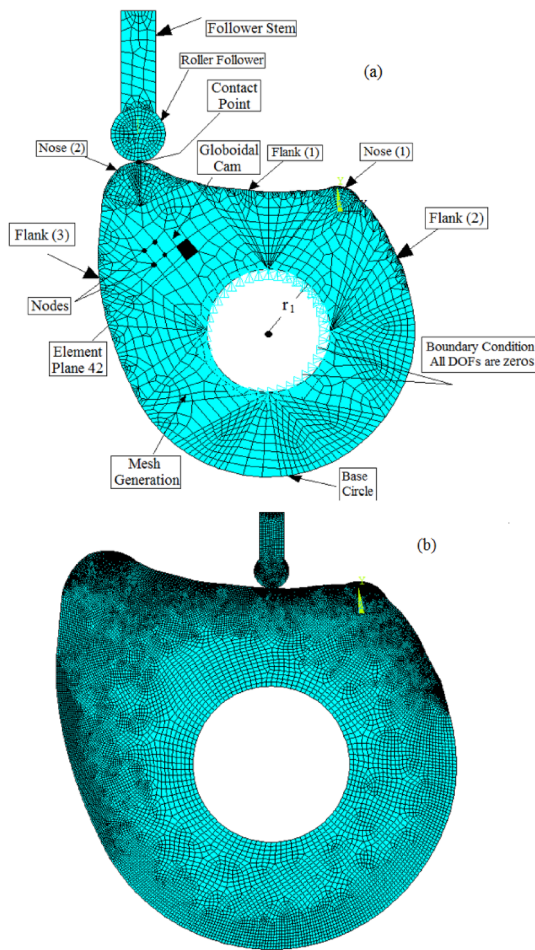


Fig. 4 Mesh generation of the finite element analysis

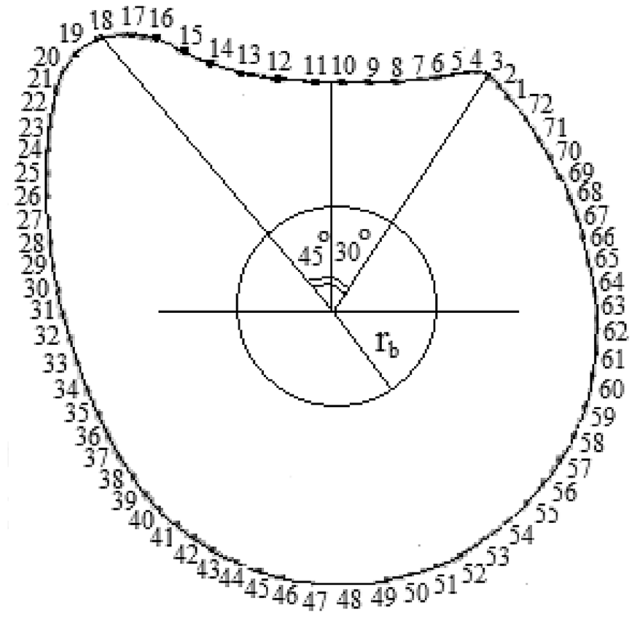


Fig. 5 Points of contact for cam profile

7 Calculation of bending deflection using ANSYS

The graphical user interface was used by ANSYS to calculate the bending deflection of the cam profile boundaries for path no. (1), path no. (2), and path no. (3). Each point in Fig. 5 was determined in ANSYS based on the position (nose or flank) and the dimension (r and θ). The following process was utilized as below: (1) Click on preference and select structural. (2) Click on preprocessor to select the element type>Add/Edit/Delete and select either element (SHELL99) or element (PLANE42) from ADD button. (3) Click on Material Props to select the material properties>Material Models>Structural>Linear>Elastic>Isotropic>Put Modulus of elasticity ($E_x = 206$ GPa), Poisson's Ratio ($PRXY = 0.29$) and the Density ($DENS = 7850$ kg/m³). (4) Click on Preprocessor>Modeling>Create and Operate to draw the 2-D globoidal cam geometry. (5) Click on Preprocessor>Meshing>Mesh Tool for the mesh generation of the cam geometry. (6) Click on Solution>Define Loads>Apply>Structural>Displacement>On Nodes and put all the degrees of freedom (translation and rotation) equal to zero around hub radius. (7) Click on Solution>Analysis Type>New Analysis>Select Harmonic. (8) Click on Solution>Define Loads>Apply>Structural>Force/Moment>On Nodes and put the maximum contact load. (9) Click on Solution>Load Step Opts>Freq and Substeps>put the harmonic frequency range between (0–10000 Hz) and Number of Substeps (100). (10) Click on Solution>Solve>Current LS to solve for the harmonic amplitude of bending deflection. (11) Click on

TimeHistPostpro>Add Data>Dof Solutuin>Select the component of displacement> Select the node on the cam profile to calculate the bending deflection.

8 Contact load formulation

The disc cam and the roller follower were assumed to be parallel cylinders with the length of (L = 10 mm) for the calculation of contact load. The roller follower radius is (R₂ = 11 mm), while the disc cam has different radius of curvatures at the points of contact (R₁ = 10, 96, 15, 126, 58, 84 mm), as shown in Fig. 3. Convex surfaces of cam profile have positive radius of curvature while the concave surfaces have negative [31]. The contact pressure was represented by the semi-ellipsoid or elliptical regions as indicated in Fig. 6 [32, 33]. This small region exhibits a very high contact stress during the active region of the cam, when the most significant loading of the followers occurs [6]. As mentioned in earlier section, both the cam and the follower were made of mild carbon steel and the plastic deformation starts when the contact pressure reaches (2.8) of the yield stress. The yield stress of mild carbon steel was at 370 MPa [34]

The maximum contact load was given by [33]:

$$P_o = \frac{3P}{2\pi a_1 b_1}, \tag{13}$$

where:

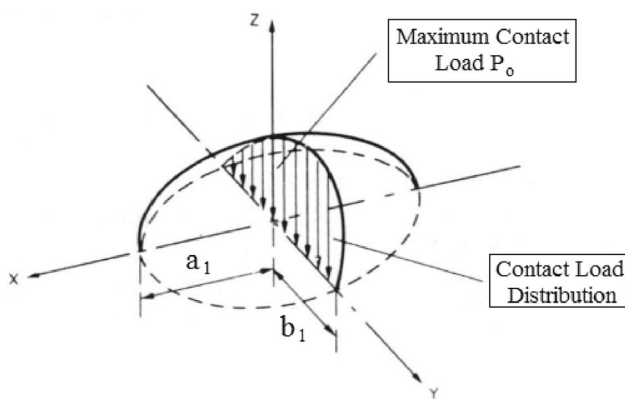


Fig. 6 Contact load distribution between the two curved bodies [34]

Table 1 Values of m₁ & n₁ for different values of angle of contact α [34]

α°	20	30	40	50	60	70	80	90
m ₁	3.778	2.731	2.136	1.754	1.486	1.284	1.128	1
n ₁	0.408	0.493	0.567	0.641	0.117	0.802	0.893	1

$$a_1 = m_1 \left(\frac{3P\Delta_1}{4A_1} \right)^{1/3}, b_1 = n_1 \left(\frac{3P\Delta_1}{4A_1} \right)^{1/3}, A_1 = 0.5 \left[\frac{1}{R_1} + \frac{1}{R_1'} + \frac{1}{R_2} + \frac{1}{R_2'} \right], B_1 = 0.5 \left[\left(\frac{1}{R_1} - \frac{1}{R_1'} \right)^2 + \left(\frac{1}{R_2} - \frac{1}{R_2'} \right)^2 + 2 \left(\frac{1}{R_1} - \frac{1}{R_1'} \right) \left(\frac{1}{R_2} - \frac{1}{R_2'} \right) \cos(2\psi) \right]^{0.5}, [33]$$

$$\Delta_1 = \frac{1}{E_1} (1 - \nu_1^2) + \frac{1}{E_2} (1 - \nu_2^2), \psi = \tan^{-1} \left(\frac{\dot{x}(t)}{x(t) + R_2^2} \right), [14]$$

The values of (m₁) and (n₁) were taken from Table 1 based on the pressure angle between cam and follower [34]:

where:

$$\alpha = \cos^{-1} \left(\frac{B_1}{A_1} \right) [33]$$

9 Mesh convergence test

Modal analysis of ANSYS software was used to calculate the value of natural frequency in Hz. Always the convergence test was needed to determine the size of elements at which the value of natural frequency settles down. The Finite element analysis of convergence curve defines the relationship between the grid interval and the analysis accuracy. Figure 7 show the convergence test of the natural frequency for the cam geometry versus the total number of elements. ANSYS package was used for the mesh convergence to calculate the exact value of the bending deflection. The points (18) and (4) were selected from the mesh convergence because they have the biggest values of bending deflection. Figure 8 show the convergence test

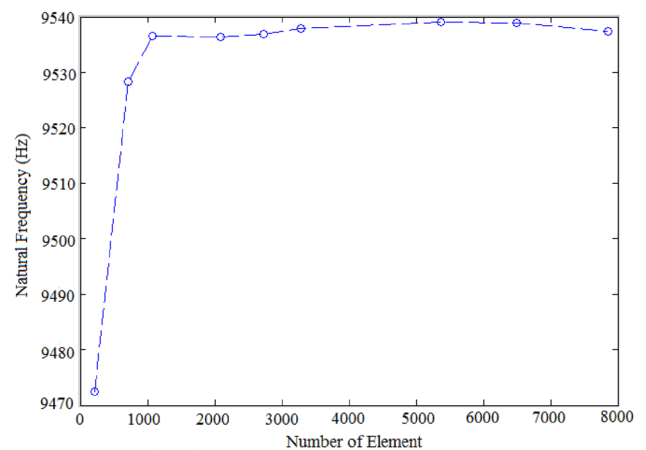


Fig. 7 Mesh convergence of modal analysis using ANSYS

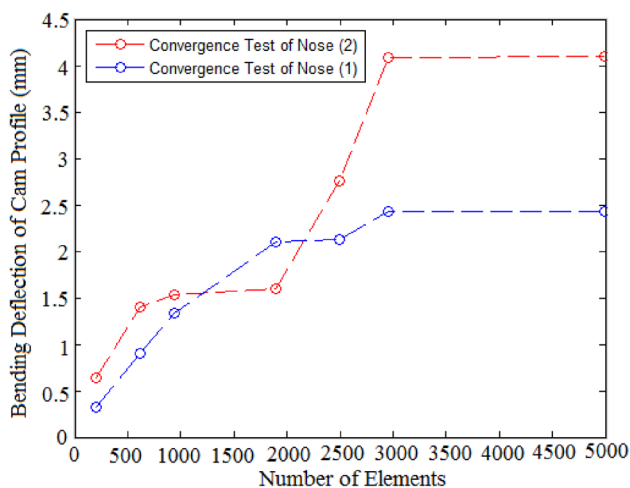


Fig. 8 Mesh convergence of bending deflection using ANSYS

of bending deflection versus the total number of elements and the points (18) and (4) were located on nose(2) and nose(1) respectively.

10 Analytic dynamic solution of bending deflection

The general equation of a circular plate in terms of r, θ, t is [35]:

$$\left(\frac{\partial^2}{\partial r^2} + \frac{2}{r}\right) * M_r + \left(-\frac{1}{r} \frac{\partial}{\partial r} + \frac{1}{r^2} \frac{\partial^2}{\partial \theta^2}\right) * M_\theta + \left(-\frac{2}{r} \frac{\partial^2}{\partial r \partial \theta} - \frac{2}{r^2} \frac{\partial}{\partial \theta}\right) * M_{r\theta} + \rho \frac{\partial^2 w}{\partial t^2} + P_o = 0, \tag{14}$$

where:

$$M_r = -D \left[\frac{\partial^2 w}{\partial r^2} + \nu_1 \left(\frac{1}{r} \frac{\partial w}{\partial r} + \frac{1}{r^2} \frac{\partial^2 w}{\partial \theta^2} \right) \right]$$

$$M_\theta = -D \left[\left(\frac{1}{r} \frac{\partial w}{\partial r} + \frac{1}{r^2} \frac{\partial^2 w}{\partial \theta^2} \right) + \nu_1 \frac{\partial^2 w}{\partial r^2} \right]$$

$$M_{r\theta} = D(1 - \nu_1) \left[\frac{1}{r} \frac{\partial^2 w}{\partial r \partial \theta} - \frac{1}{r^2} \frac{\partial w}{\partial \theta} \right]$$

$$D = \frac{E_1 h^3}{12(1 - \nu_1^2)}$$

Substituting ($M_r, M_\theta,$ and $M_{r\theta}$) into Eq. 14, one can obtain the general equation of the circular plate [35]:

$$\frac{\partial^4 w}{\partial r^4} + \frac{2}{r} \frac{\partial^3 w}{\partial r^3} - \frac{1}{r^2} \frac{\partial^2 w}{\partial r^2} + \frac{1}{r^3} \frac{\partial w}{\partial r} + \frac{2}{r^2} \frac{\partial^4 w}{\partial r^2 \partial \theta^2} - \frac{2}{r^3} \frac{\partial^3 w}{\partial r \partial \theta^2} + \frac{4}{r^4} \frac{\partial^2 w}{\partial \theta^2} + \frac{1}{r^4} \frac{\partial^4 w}{\partial \theta^4} + \frac{\rho}{D} \frac{\partial^2 w}{\partial t^2} = \frac{P_o}{D} \tag{15}$$

The homogeneous solution of Eq. (15) is [36]:

$$w(r, \theta, t)_H = \sum_{m=1,3,5}^{\infty} [A \sin(m\theta) + B \cos(m\theta)] \sin(\omega_n t), \tag{16}$$

where:

$$A = A_m r^m + B_m r^{-m} + C_m r^{m+2} + D_m r^{m-2}$$

$$B = A'_m r^m + B'_m r^{-m} + C'_m r^{m+2} + D'_m r^{m-2}.$$

For non-symmetric cam profile, the deflection, the slope, and the moment must be infinite at the center of the plate. Then the homogeneous solution of Eq. (16) is [36]:

$$w(r, \theta, t)_H = \sum_{m=1,3,5}^{\infty} [(A_m r^m + C_m r^{m+2}) \sin(m\theta) + (A'_m r^m + C'_m r^{m+2}) \cos(m\theta)] \sin(\omega_n t) \tag{17}$$

Applying the infinite series theorem on the homogeneous solution of Eq. (17), one can obtain:

$$r^m \sin(m\theta) = (1 + r + r^2 + r^3 + r^4 + r^5 + \dots)$$

$$(m\theta - \frac{(m\theta)^3}{3!} + \frac{(m\theta)^5}{5!} - \dots)$$

The cam profile is unsymmetrical (odd function) and the symmetric terms (even function) have been ignored as follows:

$$r^m \sin(m\theta) = (rm\theta) - \frac{(rm\theta)^3}{3!} + \frac{(rm\theta)^5}{5!} = \sin(rm\theta)$$

For the first mode, $m = 1$:

$$r^m \sin(m\theta) = \sin(r\theta)$$

Also the same procedure for the second term:

$$r^{m+2} \sin(m\theta) = \sin(r\theta)$$

As previously stated:

$$r^m \cos(m\theta) = (1 + r + r^2 + r^3 + r^4)$$

$$(1 - \frac{(m\theta)^2}{2!} + \frac{(m\theta)^4}{4!} - \dots) = \cos(r\theta),$$

and

$$r^{m+2} \cos(m\theta) = \cos(r\theta)$$

The homogeneous solution of Eq. (17) is [36]:

$$w(r, \theta, t)_H = [A \sin(r\theta) + B \cos(r\theta)] \sin(\omega_n t), \tag{18}$$

where: A and B are constants.

The particular solution is [36]:

$$w(r, \theta, t)_p = \sum_{m=1,3,5}^{\infty} [Cr^4 \sin(m\theta)] \sin(\Omega t), \tag{19}$$

where C is constant of particular solution.

By applying the infinite series theorem on the particular solution of Eq. (19), the following relation was obtained:

$$r^4 \sin(m\theta) = (1 + r + r^2 + r^3 + r^4 + \dots) \left(m\theta - \frac{(m\theta)^3}{3!} + \frac{(m\theta)^5}{5!} \right).$$

The higher order terms were ignored and the non-symmetric terms were taken into account. For the first mode, $m = 1$:

$$r^4 \sin(m\theta) = rm\theta$$

The particular solution of Eq. (19) will become:

$$w(r, \theta, t)_p = Cr\theta \sin(\Omega t) \tag{20}$$

Substitute Eq. (20) into Eq. (15), the particular solution of Eq. (20) will be:

$$w(r, \theta, t)_p = \left[\frac{P_o R_p^3}{\theta_p D} + \frac{\rho \Omega^2 R_p^3}{\theta_p D} \right] r\theta \sin(\Omega t). \tag{21}$$

The general solution of the bending deflection of the cam profile given by Eq. (15) was:

$$w(r, \theta, t) = [A \sin(r\theta) + B \cos(r\theta)] \sin(\omega_n t) + \left[\frac{P_o R_p^3}{\theta_p D} + \frac{\rho \Omega^2 R_p^3}{\theta_p D} \right] r\theta \sin(\Omega t) \tag{22}$$

The boundary conditions were applied on Eq. (22) and it had been obtained the constants (A) and (B) as in below:

$$At(r = r_1), (\theta = \theta_p), t = t_1, w(r, \theta, t) = 0,$$

$$At(r = r_1), (\theta = \theta_p), t = t_1, \frac{\partial w(r, \theta, t)}{\partial r} = 0.$$

The constants (A & B) were as follows:

$$A = - \left(\frac{P_o R_p^3}{\theta_p D} + \frac{\rho \Omega^2 R_p^3}{\theta_p D} \right) (r_1 \theta_p \sin(r_1 \theta_p) + \cos(r_1 \theta_p)) \frac{\sin(\Omega t_1)}{\sin(\omega_n t_1)}$$

$$B = \left(\frac{P_o R_p^3}{\theta_p D} + \frac{\rho \Omega^2 R_p^3}{\theta_p D} \right) (\sin(r_1 \theta_p) - \theta_p \cos(r_1 \theta_p)) \frac{\sin(\Omega t_1)}{\sin(\omega_n t_1)}$$

The general solution of bending deflection of cam profile at the point of contact is:

$$w(r, \theta, t) = - \left(\frac{P_o R_p^3}{\theta_p D} + \frac{\rho \Omega^2 R_p^3}{\theta_p D} \right) \frac{\sin(\Omega t_1)}{\sin(\omega_n t_1)} (-r_1 \theta_p \sin(r_1 \theta_p) \sin(r\theta) - \cos(r_1 \theta_p) \sin(r\theta) + \sin(r_1 \theta_p) \cos(r\theta) - \theta_p \cos(r_1 \theta_p) \cos(r\theta)) \sin(\omega_n t) + \left[\frac{P_o R_p^3}{\theta_p D} + \frac{\rho \Omega^2 R_p^3}{\theta_p D} \right] r\theta \sin(\Omega t) \tag{23}$$

where:

$$t_1 = \frac{\theta_p}{\Omega}$$

11 Results and discussions

Figure 9 shows the bending deflection versus the angle of contact for path no. (1), path no. (2), and path no. (3). The bending deflection of path no. (2) and path no. (3) varied sinusoidal with the increasing of the angle of contact.

Figure 10 shows the contact load versus the angle of contact for path no. (1), path no. (2), and path no. (3). The contact load of path no. (1) and path no. (2) is increasing with the increase of the angle of contact, while the contact load of path no. (3) is decreasing with the increase of the angle of contact.

Tables 2, 3 and 4 show the verification of bending deflection of path no. (1), path no. (2), and path no. (3) of cam profile respectively. The verification has been done using a spring-damper system and the cam angular velocity is $N = 500$ rpm. In ANSYS, the area of contact between the cam and the follower was assumed to

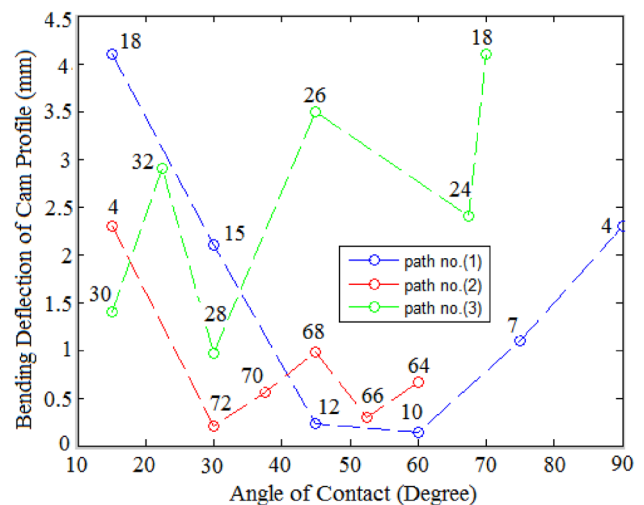


Fig. 9 Bending deflection of path no. (1), path no. (2), and path no. (3)

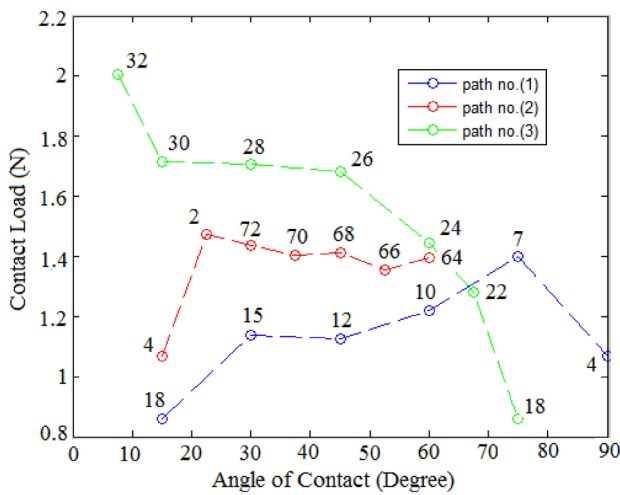


Fig. 10 Contact load of path no. (1), path no. (2), and path no. (3)

Table 2 Verification of bending deflection for path no. (1) of cam profile

Contact points	Analytic (mm)	ANSYS (mm)	Error (%)
4	2.3	2.4318	5.419
7	1.1	1.0579	3.287
10	0.14116	0.15488	8.858
12	0.2288	0.223	2.535
15	2.1	2.2124	5.080
18	4.1	4.369	6.157

Table 3 Verification of bending deflection for path no. (2) of cam profile

Contact points	Analytic (mm)	ANSYS (mm)	Error (%)
4	2.3	2.4318	5.419
72	0.20594	0.22022	6.818
70	0.55368	0.60284	8.319
68	0.9772	1.0091	2.300
66	0.28965	0.26712	7.612
64	0.66408	0.62061	6.626

be rectangular. For the analytic solution of Eq. (23), the contact was assumed to be a volume of a small elliptical region (contact between two curved surfaces).

Table 5, 6, and 7 show the contact area for path no. (1), path no. (2), and path no. (3) before and after using spring-damper system.

Figures 11, 12 and 13 show the verification of the bending deflection versus the angle of contact of path

Table 4 Verification of bending deflection for path no. (3) of cam profile

Contact points	Analytic (mm)	ANSYS (mm)	Error (%)
32	1.4	1.2968	7.857
30	2.9	2.6587	8.620
28	0.96255	0.99958	3.703
26	3.5	3.181	8.571
24	2.4	2.265	5.833
18	4.1	4.369	6.157

Table 5 Area of contact before and after using spring-damper system for Path no. (1)

Contact points	Contact area before	Contact area after
4	0.201	0.173
7	0.500	0.312
10	0.610	0.463
12	0.395	0.255
15	0.401	0.324
18	0.304	0.225

Table 6 Area of contact before and after using spring-damper system for Path no. (2)

Contact points	Contact area before	Contact area after
4	0.490	0.150
72	0.598	0.194
70	0.556	0.215
68	0.462	0.346
66	0.503	0.141

Table 7 Area of contact before and after using spring-damper system for Path no. (3)

Contact points	Contact area before	Contact area after
32	0.607	0.361
28	0.499	0.357
24	0.499	0.351
18	0.229	0.188

no. (1), path no. (2), and path no. (3). In general, the analytic results are very close to the ANSYS results. In Fig. 11 the maximum difference between the two sets of results is (8.858%) at point (10), while in Fig. 12 the maximum difference is (8.319%) at point (70). In Fig. 13 the maximum difference between the two sets of results is (8.620%) at point (30).

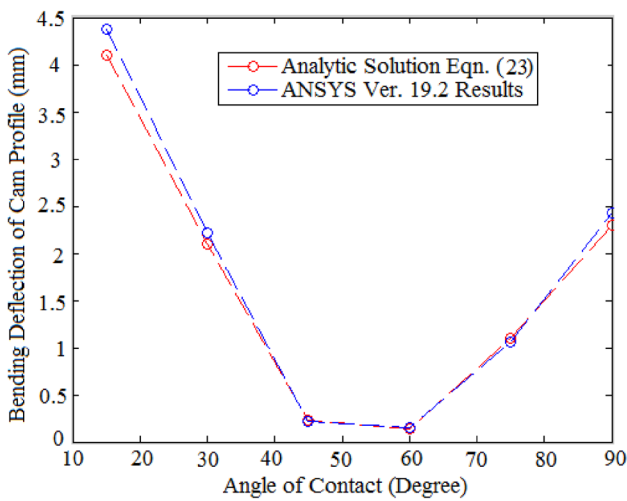


Fig. 11 Verification of Bending deflection for path no. (1)

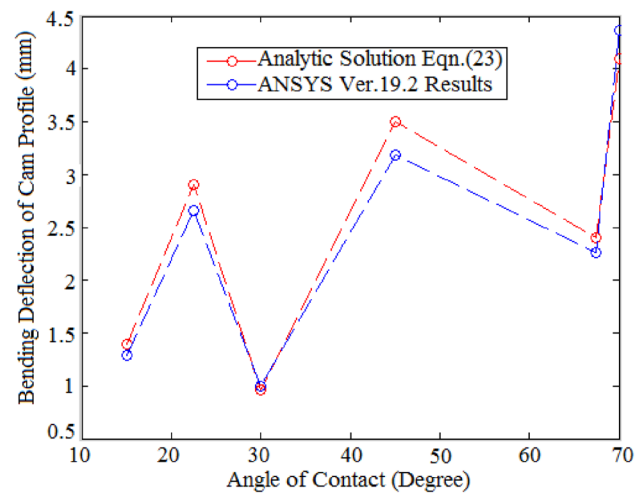


Fig. 13 Verification of Bending deflection for path no. (3)

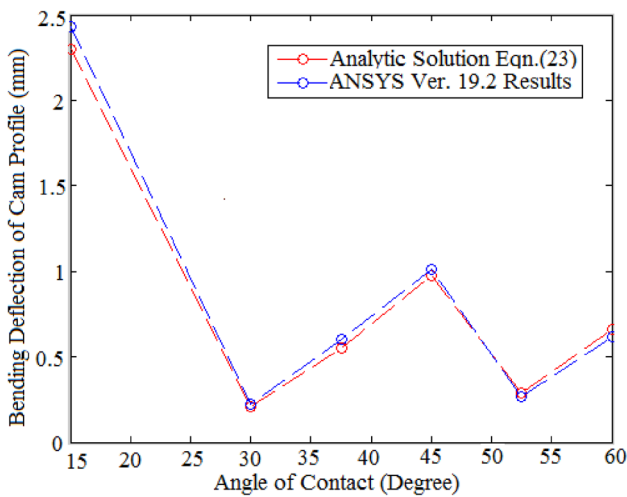


Fig. 12 Verification of Bending deflection for path no. (2)

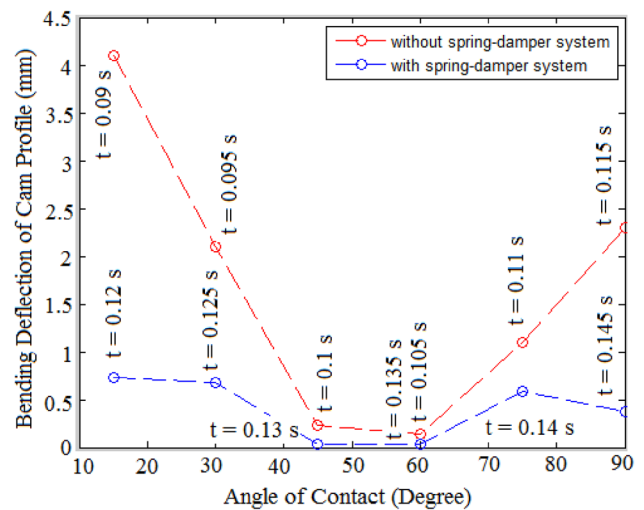


Fig. 14 Bending deflection versus the angle of contact for path no. (1) using and without using spring-damper system

Figures 14, 15 and 16 show the bending deflection of cam profile versus the angle of contact at each time step for path no. (1), path no. (2), and path no. (3) with and without the spring-damper system. The bending deflection is reduced to (82.101%, 67.478%, 87.558%, 72.983%, 46.691%, 83.743%) for the points (18,15,12,10,7,4) on path no. (1). The bending deflection is reduced to (90.167%, 80.754%, 96.771%, 82.898%, 79.035%) for the points (72,70,68,66,64) on path no. (2).

More over, the bending deflection is reduced to (85.601%, 31.034%, 54.179%, 60%, 76.522%) for the points (32,30,28,26,24) on path no. (3).

Figures 17, 18 and 19 show the contact load versus the angle of contact of path no. (1), path no. (2), and path no. (3) with and without the spring-damper system. The

contact load is reduced to (21.673%, 28.275%, 27.643%, 24.952%, 33.194%, 30.36%) for the points (18,15,12,10,7,4) on path no. (1). The contact load is reduced to (45.092%, 33.222%, 31.145%, 34.282%, 29.313%) for the points (72,70,68,66,64) on path no. (2). More over, the contact load is reduced to (37.784%, 37.968%, 37.941%, 41.907%, 34.842%) for the points (32, 30, 28, 26, 24) on path no. (3).

Figure 20a shows the dynamic response of the follower versus the angle of contact for one cycle of cam rotation. The cam profile with rise-return-rise-return-dwell-rise was selected for this study. The cam starts rotating with a rise motion for (45 degrees) followed by a return stroke with (30 degrees). A rise stroke for the next (35 degrees) and a return stroke with (40 degrees).

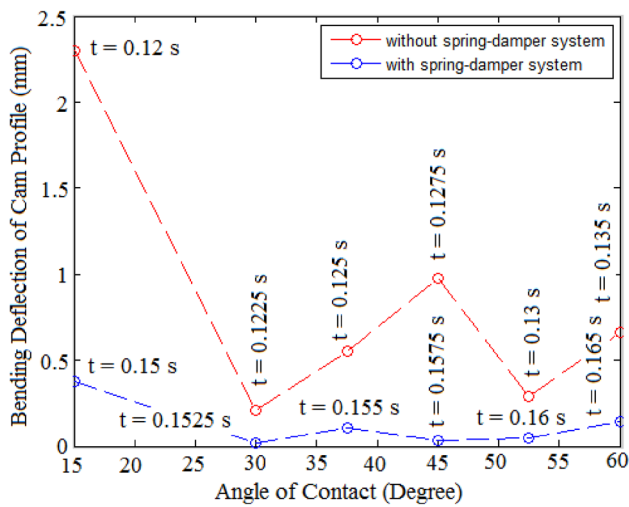


Fig. 15 Bending deflection versus the angle of contact for path no. (2) using and without using spring-damper system

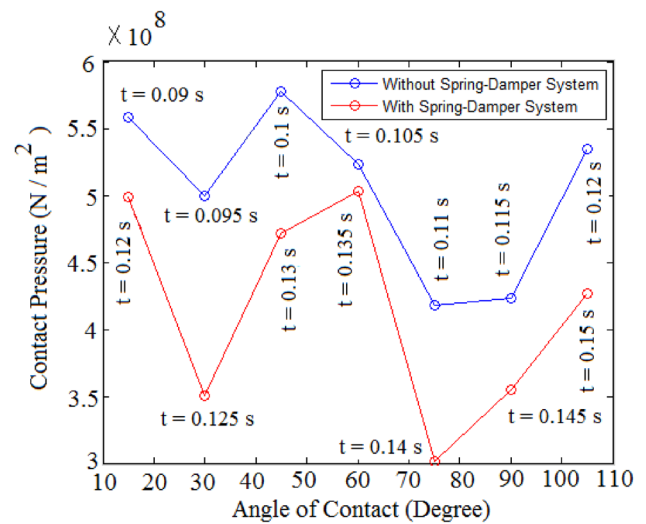


Fig. 17 Contact load versus the angle of contact for path no. (1) using and without using spring-damper system

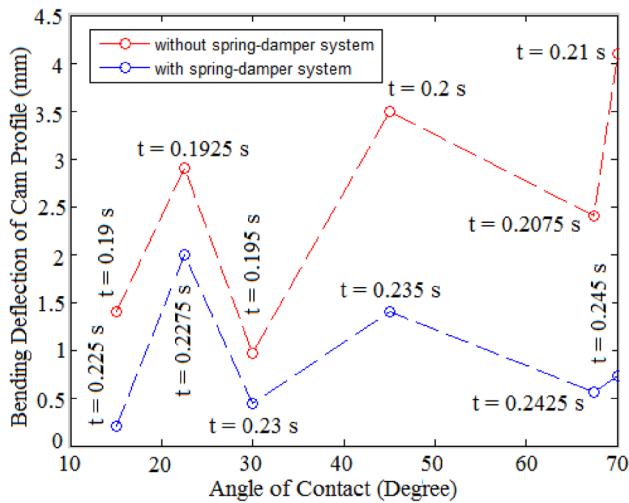


Fig. 16 Bending deflection versus the angle of contact for path no. (3) using and without using spring-damper system

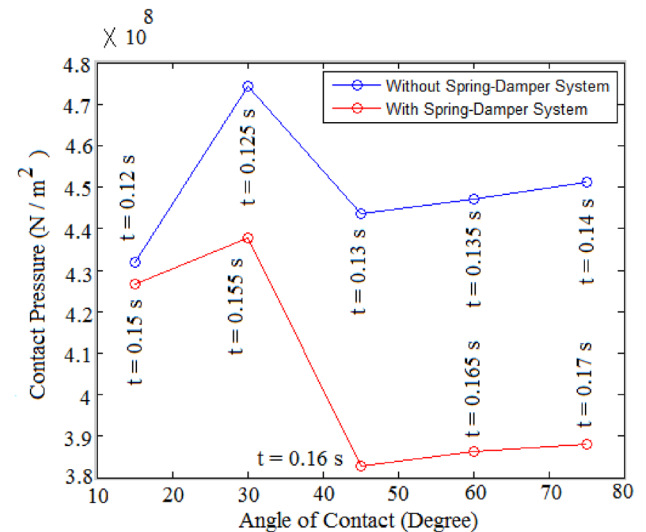


Fig. 18 Contact load versus the angle of contact for path no. (2) using and without using spring-damper system

A dwell motion for the next (180 degrees) was designed to retain the contact between the cam and the follower. The cam is ending one cycle of rotation with the rise stroke for the next (30 degrees). Analytic solution of Eq. 7, SolidWorks simulation, and experiment setup were used to verify the dynamic response of the follower. Figure 20b shows the analytic result of the variation of the dynamic response of the follower based on the increase of the viscous damping coefficient from 0.875 to 1 and

the spring stiffness from 7 to 10. The dynamic response is decreasing with the increase of the spring stiffness and the viscous damping coefficient values.

Figure 21 shows the amplitude of the bending deflection of cam profile versus the frequency for the points (18) and (4) on nose(2) and nose(1) respectively. Harmonic analysis was performed to find the dynamic response of the bending deflection at the natural frequency (9538 Hz) using ANSYS. The amplitude peak of the point (18)

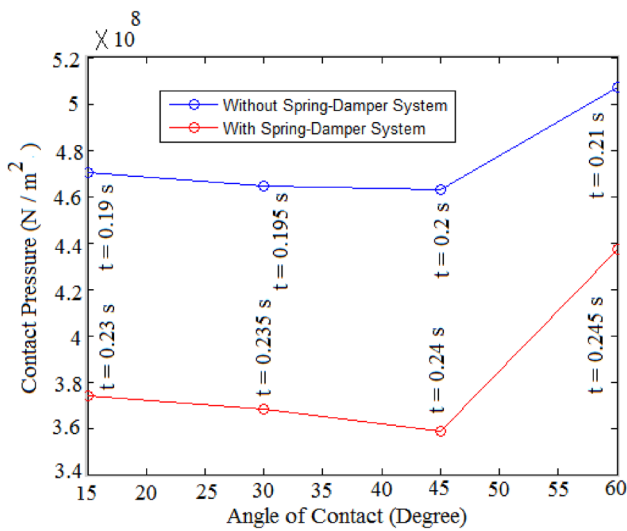


Fig. 19 Contact load versus the angle of contact for path no. (3) using and without using spring-damper system

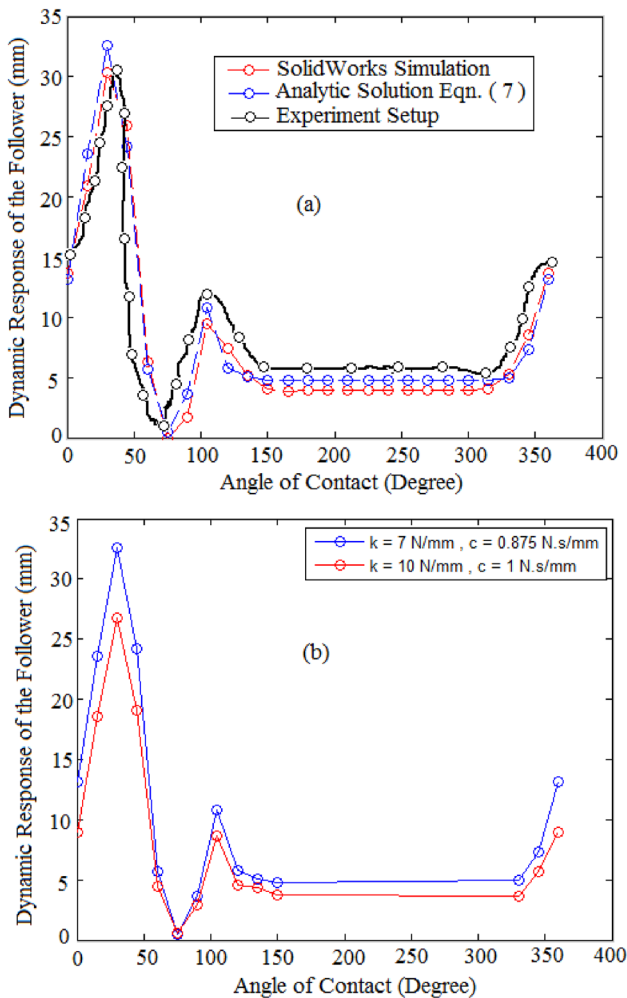


Fig. 20 Verification of dynamic response for the follower

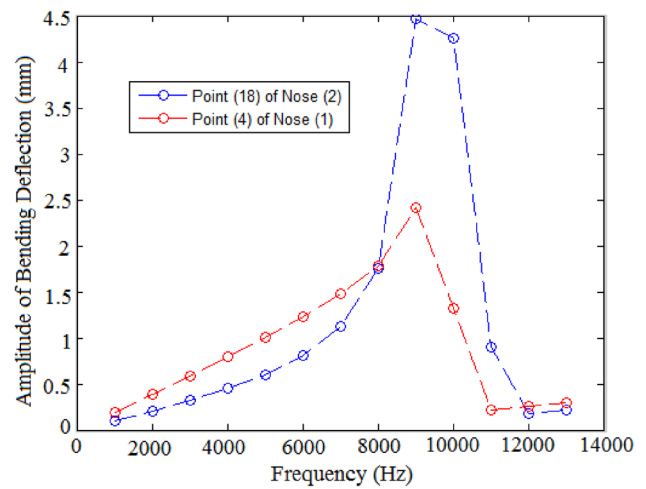


Fig. 21 Harmonic analysis of bending deflection of cam profile

on nose(2) is bigger than the peak of point (4) on nose(1) because of large values of radius of curvature of nose(2).

Figure 22 shows the variation of the major and the minor axes of the Hertzian contact ellipse against the contact angle for path no. (1), path no. (2), and path no. (3) respectively. All the values of major axes are increasing with the increase of the angle of the contact for path no. (1) and path no. (2) while the major axes for path no. (3) are decreasing with the increase of the contact angle. Moreover, all the values of minor axes are decreasing with the increasing of the angle of contact for path no. (1) and path no. (2) while the minor axes for path no. (3) are increasing with the increase of the contact angle.

Figure 23 shows the contact load simulation between cam and follower for greasy and dry friction. Contact load simulation has been done using SolidWorks. The values of contact load for dry and greasy friction are almost the same.

Figure 24 shows the convergence test of Von Mises stress against the total number of elements for nose(2) and nose(1) using the spring-damper system. The points (18) and (4) were located at nose(2) and nose(1) respectively.

12 Conclusions

The major findings of this study is how to reduce the bending deflection and the contact load of the cam profile at the point of contact. The relevance of this work comes through an addition of spring-damper system at the end of follower stem to keep the bending deflection and the contact load as low as possible. The reduction rate for bending deflection is (73.425%) for path no. (1), (85.925%)

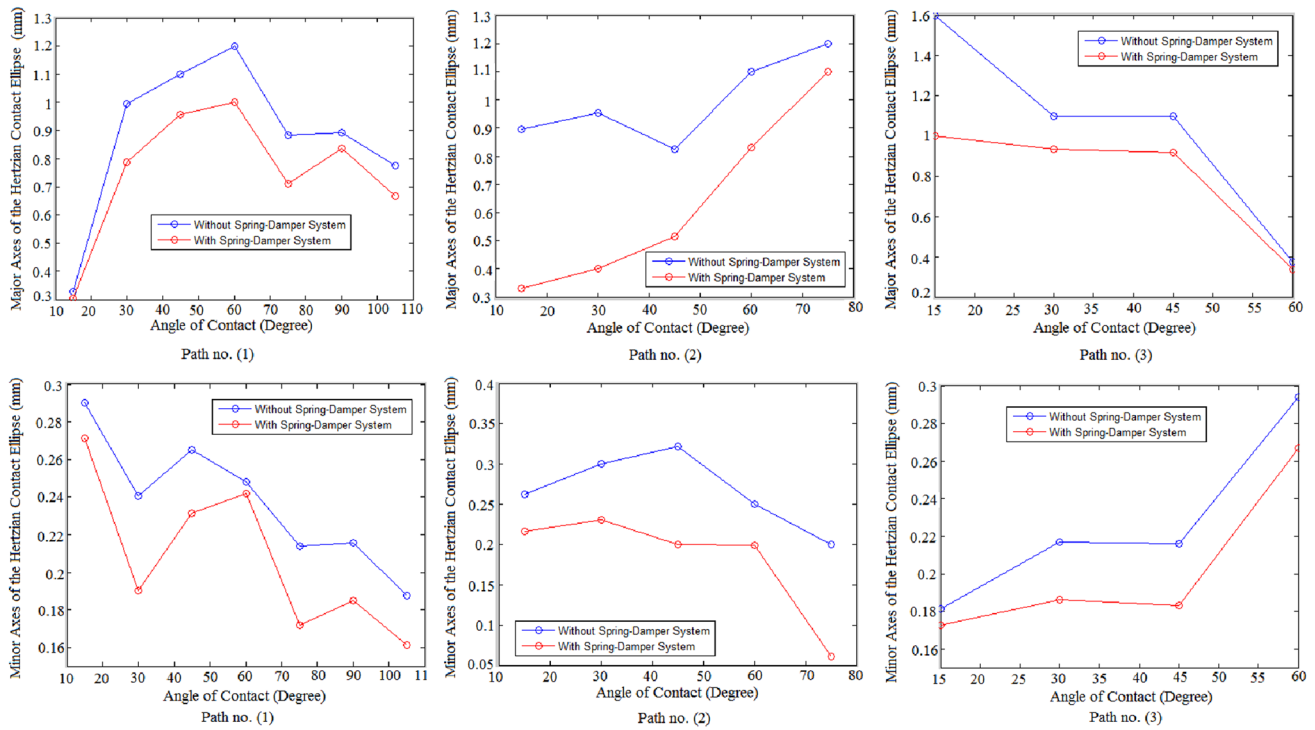


Fig. 22 Major and minor axes of the Hertzian Contact Ellipse

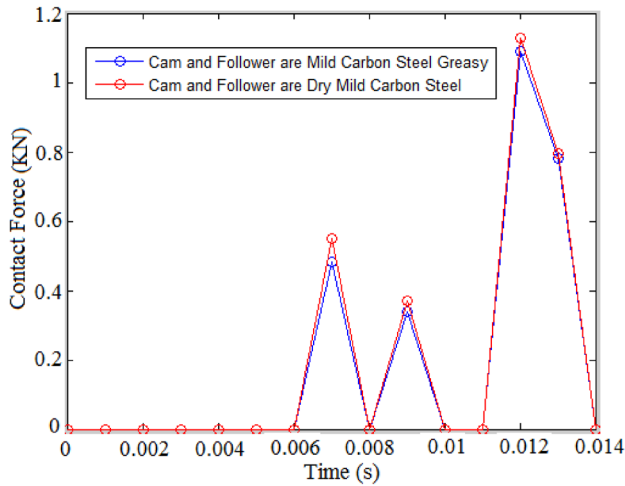


Fig. 23 Contact load simulation for greasy and dry friction

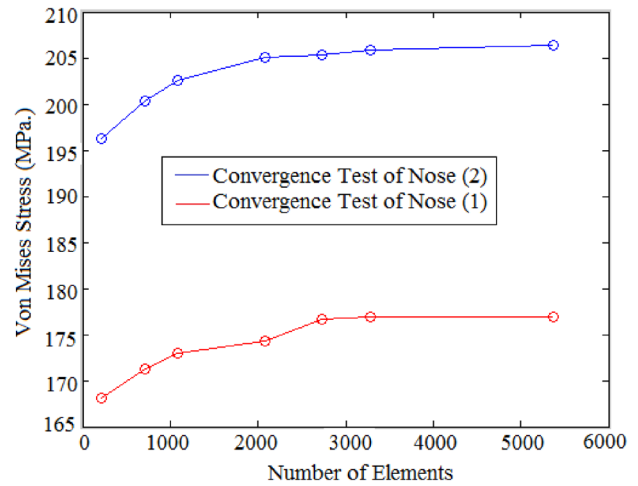


Fig. 24 Convergence test of Von Mises Stress using ANSYS software

for path no. (2), and (61.467%) for path no. (3). The reduction rate for contact load is (27.682%) for path no. (1), (34.61%) for path no. (2), and (38.088%) for path no. (3). The limitation of this work is how to measure the contact load experimentally at the point of contact. In regards the

future work, genetic algorithm technique can be used to reduce the bending deflection and the contact of the cam profile.

Acknowledgements We want to first thank the reviewers and the editor for reviewing our paper.

Compliance with ethical standards

Conflict of interest The authors declare that they have no conflict of interest.

References

1. Sundar S, Dreyer JT, Singh R (2013) Rotational sliding contact dynamics in a non-linear cam-follower system as excited by a periodic motion. *J Sound Vib* 332(18):4280–4295
2. Machado M, Moreira P, Flores P, Lankarani HM (2012) Compliant contact force models in multibody dynamics: evolution of the hertz contact theory. *Mech Mach Theory* 53:99–121
3. Kuang J-H, Hsu C-M, Hu C-C (2010) Dynamic behavior of globoidal cam systems with torque compensation mechanisms. *Mech Mach Theory* 45(8):1201–1214
4. Hsieh J-F, Hsieh W-C (2016) Design of cam mechanism with negative radius roller-follower. In: MATEC web of conferences, vol 71. EDP Sciences, p 04003
5. Hua D, Farhang K, Seitzman L (2007) A multi-scale system analysis and verification for improved contact fatigue life cycle of a cam-roller system. *J Tribol* 129(2):321–325
6. Lahr DF, Hong DW (2007) Contact stress reduction mechanisms for the cam-based infinitely variable transmission. In: ASME 2007 international design engineering technical conferences and computers and information in engineering conference. American Society of Mechanical Engineers, pp 449–456
7. Ghazalli MHB (2007) Finite element analysis of cam and its follower contact stress mechanism. Ph.D. thesis, UMP
8. Fabien B, Longman R, Freudenstein F (1994) The design of high-speed dwell-rise-dwell cams using linear quadratic optimal control theory. *J Mech Des* 116(3):306–310
9. Sahu LK, Gupta OP, Sahu M (2016) Design of cam profile using higher order b-spline. *Int J Innocative Sci Eng Technol* 3(2):327–335
10. Angeles J, Saha S, López Cajún C (1994) The design of cam mechanisms with translating flat-face followers under curvature constraints. *J Mech Des* 116(1):306–310
11. Chew M, Freudenstein F, Longman R (1983) Application of optimal control theory to the synthesis of high-speed cam-follower systems. part 2: system optimization. *J Mech Trans Autom* 105(3):585–591
12. Pandey D, Sinha PK, Prakash EV (2015) Analysis and study of cam and follower through ansys and artificial neural network. *Int J Eng Sci* 4(7):1–8
13. Al-Shamma F, Mustafa FF, Saliman SM (2010) An optimum design of cam mechanisms with roller follower for combined effect of impact and high contact loads. *Al-Khwarizmi Eng J* 6(4):62–71
14. Tsiafis I, Mitsi S, Bouzakis K, Papadimitriou A (2013) Optimal design of a cam mechanism with translating flat-face follower using genetic algorithm. *J Tribol Ind* 35(4):255–260
15. Patel MN (2015) Modelling, design and analysis of cam and follower—a review paper. *Int J Eng Stud Techn Approach* 1(2):36–42
16. Himelblau H, Wise J, Piersol A, Grundvig MR (1994) Handbook for dynamic data acquisition and analysis-IES recommended practices 012.1
17. Yousuf LS (2019) Experimental and simulation investigation of nonlinear dynamic behavior of a polydyne cam and roller follower mechanism. *Mech Syst Signal Process* 116:293–309
18. Vela D, Ciulli E, Piccigallo B, Fazzolari F (2011) Investigation on cam-follower lubricated contacts. *Proc Inst Mech Eng J J Eng Tribol* 225(6):379–392
19. Parador V (2007) An impact model for the industrial cam-follower system: simulation and experiment
20. Belliveau KD (2002) An investigation of incipient jump in industrial cam follower systems. Ph.D. thesis, Worcester Polytechnic Institute
21. Rothbart HA, Klipp DL (2004) Cam design handbook, vol 394. McGraw-Hill, New York
22. Felszeghy SF (2005) Steady-state residual vibrations in high-speed, dwell-type, rotating disk cam-follower systems. *J Vib Acoust* 127(1):12–17
23. Rao SS, Gavane S (1982) Analysis and synthesis of mechanical error in cam-follower systems. *J Mech Des* 104(1):52–62
24. Planchard D (2017) SOLIDWORKS 2017 reference guide. SDC Publications, Mission
25. Uicker JJ, Pennock GR, Shigley JE et al (2011) Theory of machines and mechanisms, vol 1. Oxford University Press, New York
26. Yousuf LS, Marghitu DB (2017) Non-linear dynamic analysis of a cam with flat-faced follower linkage mechanism. In: ASME 2017 international mechanical engineering congress and exposition. American Society of Mechanical Engineers Digital Collection
27. Shigley JE (2011) Shigley's mechanical engineering design. Tata McGraw-Hill Education, New York
28. Slocum AH (1992) Precision machine design. Society of Manufacturing Engineers, Southfield
29. Gheadnia H, Cermik O, Marghitu DB (2015) Experimental and theoretical analysis of the elasto-plastic oblique impact of a rod with a flat. *Int J Impact Eng* 86:307–317
30. Thompson MK, Thompson JM (2017) ANSYS mechanical APDL for finite element analysis. Butterworth-Heinemann, Oxford
31. Bhushan B (2013) Introduction to tribology. Wiley, Hoboken
32. Bhushan B (2000) Modern tribology handbook, two volume set. CRC Press, Boca Raton
33. Beer F, DeWolf J, Johnston ER Jr, Mazurek D (2014) Mechanics of materials. McGraw-Hill Education, New York
34. EJ, H, (1959) Mechanics of materials. McGraw-Hill Education, New York
35. Szilard R (2004) Theories and applications of plate analysis: classical, numerical and engineering methods. Wiley, Hoboken
36. Timoshenko SP, Woinowsky-Krieger S (1959) Theory of plates and shells. McGraw-hill, New York

Publisher's Note Springer Nature remains neutral with regard to jurisdictional claims in published maps and institutional affiliations.